

This article was downloaded by: [Ecole Centrale Paris]

On: 15 December 2008

Access details: Access Details: [subscription number 790383386]

Publisher Taylor & Francis

Informa Ltd Registered in England and Wales Registered Number: 1072954 Registered office: Mortimer House, 37-41 Mortimer Street, London W1T 3JH, UK



## Combustion Theory and Modelling

Publication details, including instructions for authors and subscription information:

<http://www.informaworld.com/smpp/title-content=t713665226>

### Triple flame propagation and stabilization in a laminar axisymmetric jet

Xiao Qin <sup>a</sup>; Chun W. Choi <sup>b</sup>; Achintya Mukhopadhyay <sup>c</sup>; Ishwar K. Puri <sup>a</sup>; Suresh K. Aggarwal <sup>a</sup>; Viswanath R. Katta <sup>c</sup>

<sup>a</sup> Department of Mechanical and Industrial Engineering m/c 251, University of Illinois at Chicago, Chicago, IL, USA <sup>b</sup> Mechanical Engineering Department, Jadavpur University, Calcutta 700-032, India <sup>c</sup> Innovative Scientific Solutions, Inc., Dayton, Ohio, USA

Online Publication Date: 26 March 2004

**To cite this Article** Qin, Xiao, Choi, Chun W., Mukhopadhyay, Achintya, Puri, Ishwar K., Aggarwal, Suresh K. and Katta, Viswanath R. (2004) 'Triple flame propagation and stabilization in a laminar axisymmetric jet', *Combustion Theory and Modelling*, 8:2, 293 — 314

**To link to this Article:** DOI: 10.1088/1364-7830/8/2/006

**URL:** <http://dx.doi.org/10.1088/1364-7830/8/2/006>

PLEASE SCROLL DOWN FOR ARTICLE

Full terms and conditions of use: <http://www.informaworld.com/terms-and-conditions-of-access.pdf>

This article may be used for research, teaching and private study purposes. Any substantial or systematic reproduction, re-distribution, re-selling, loan or sub-licensing, systematic supply or distribution in any form to anyone is expressly forbidden.

The publisher does not give any warranty express or implied or make any representation that the contents will be complete or accurate or up to date. The accuracy of any instructions, formulae and drug doses should be independently verified with primary sources. The publisher shall not be liable for any loss, actions, claims, proceedings, demand or costs or damages whatsoever or howsoever caused arising directly or indirectly in connection with or arising out of the use of this material.

## Triple flame propagation and stabilization in a laminar axisymmetric jet

Xiao Qin<sup>1,4</sup>, Chun W Choi<sup>1</sup>, Achintya Mukhopadhyay<sup>2</sup>,  
Ishwar K Puri<sup>1,5</sup>, Suresh K Aggarwal<sup>1</sup> and Viswanath R Katta<sup>3</sup>

<sup>1</sup> Department of Mechanical and Industrial Engineering m/c 251, University of Illinois at Chicago, 842 W. Taylor St, Chicago, IL 60607-7022, USA

<sup>2</sup> Mechanical Engineering Department, Jadavpur University, Calcutta 700-032, India

<sup>3</sup> Innovative Scientific Solutions, Inc., Dayton, Ohio 45440, USA

E-mail: ikpuri@uic.edu

Received 15 July 2003, in final form 2 February 2004


Published 26 March 2004

Online at [stacks.iop.org/CTM/8/293](http://stacks.iop.org/CTM/8/293)

DOI: 10.1088/1364-7830/8/2/006

### Abstract

The propagation of a methane–air triple flame in a partially premixed jet is investigated experimentally and numerically. The flame is ignited with a Nd:YAG laser in a nonuniform jet-mixing layer downstream of the burner. The ignition and flame propagation processes are recorded using a high-speed video camera. The flamefront propagation velocity in laboratory coordinates is inferred from the video images. A comprehensive, time-dependent computational model is used to simulate the transient ignition and flame propagation phenomena. The model employs a detailed description of methane–air chemistry and transport properties. Following ignition, a well-defined triple flame is formed that propagates upstream towards the burner along the stoichiometric mixture fraction line. As the flame propagates upstream, the flame propagation speed, which is defined as the normal flamefront velocity with respect to the local gas velocity, decreases linearly. Near the burner wall, the flame curvature increases to two times the value of its downstream freely propagating counterpart. During the flame propagation process, the curvature-induced stretch dominates over the hydrodynamic stretch and the flame speed decreases with increasing stretch rate in accord with previous measurements. We also examine the dominant reaction rates to follow the transition from a triple flame to a double flame structure.

 This article features online multimedia enhancements

(Some figures in this article are in colour only in the electronic version)

<sup>4</sup> Present address: Department of Mechanical and Aerospace Engineering, Princeton University, Princeton, NJ 08540, USA.

<sup>5</sup> Author to whom any correspondence should be addressed.

## 1. Introduction

Since the first publication, by Phillips [1], that described a triple flame in a mixing layer, triple flame behaviour has been extensively investigated because of the important role of these flames during flame stabilization, flame spread, and re-ignition in turbulent combustion [2]. Kioni *et al* [3] and Plessing *et al* [4] investigated the formation of triple flames in a nitrogen-diluted methane stream. They concluded that the existence of a fuel mass fraction gradient normal to the flow direction, along which the equivalence ratio varies from fuel rich to fuel lean, is an essential condition for the formation of a triple flame. This ability to propagate in a nonuniform mixture is an important characteristic of a triple flame.

Partially premixed flames occur in many combustion devices, such as various industrial burners, and internal combustion and aircraft engines [5]. A fault or instability in these systems can induce local flame extinction or blow out, followed by a re-ignition event. The process of re-ignition can involve the formation of a triple flame that may lose its characteristics during propagation [2]. Under certain conditions a propagating triple flame may lose one or both of its premixed wings and degrade into a double or diffusion flame [6, 7]. This transition is of both fundamental and practical interest and it is worth verifying the validity of the various theories that seek to explain this phenomenon.

Hartley and Dold [8] and Ruetsch *et al* [9] have reported analytical and numerical investigations of triple flame propagation in nonuniform mixtures. They found that the flame propagation speed decreases as the mixture fraction gradient increases. However, their results were obtained using a single-step global reaction model with idealized assumptions that ignored the effects of unequal species diffusivities. Furthermore, realistic flames are stretched and experience time-varying mixture fraction gradients and changes in their shape and curvature—factors that have not previously been addressed in detail. Echehki and Chen [10] numerically investigated the influence of gravity in the upward and downward propagation and structure of triple flames. However, they too considered single-step chemistry and diffusively neutral mixtures. Their investigation considered freely propagating triple flames and, therefore, those results are inapplicable for flames propagating in the proximity of a burner.

Kioni *et al* [3] conducted a numerical investigation of a propagating triple flame, and observed that with increasing strain rate the complex structure of a triple flame transforms into that of a conventional nonpremixed (NP) flame. Using the concept of a transport layer, Wichman [11] demonstrated that near a burner wall the premixed flame wing of a triple flame becomes a ‘flame nub’ due to heat losses to the wall. Fernandez *et al* [12] analysed the structure of NP flames near the rim of an injector and showed that the Karlovitz number plays an important role in characterizing the flame shape, and its attachment and lift-off. Im and Chen [13] investigated the effect of strain on triple flame propagation and showed that the precise identification of the triple point of a propagating triple flame that is subject to a large strain field becomes ambiguous. They demonstrated that large discrepancies arise in the flame propagation speeds determined at the triple point when it is variously defined as the location of the maximum curvature or of the maximum heat release.

Watson *et al* [14] and Su *et al* [15] have reported experimental investigations of lifted turbulent flames. They observed that lean-premixed (LP) and NP reaction zones exist, but did not find a rich-premixed (RP) reaction zone in their turbulent lifted flames. They hypothesized that the RP flame branch was folded into the NP flame tail. Takahashi *et al* [16] investigated the stabilization of NP laminar flames, and also did not report a triple flame structure at the base of these lifted flames. Instead, they proposed that a reaction kernel of high reactivity provides the radical flux and serves as a stabilization point that is located

in a small premixing zone. Ko and Chung [17] investigated the propagation of laminar triple flames in NP methane jets, and examined the correlations for flame propagation speed with respect to flame curvature, stretch, and fuel mass fraction gradient. However, they focused on the far field of various axisymmetric jets and did not address the transition of a triple flame into other types of flames, such as a double flame or an edge flame near the burner rim. Moreover, the present investigation focuses on the triple flame propagation and stabilization in a partially premixed mixture. Lee *et al* [18] studied the lift-off and blow-out characteristics of laminar partially premixed jet flames of propane and *n*-butane. They found that as the extent of partial premixing increases, both the lift-off and blow-out velocities decrease and, eventually, the lifted flame was not observed for fuel mass fractions less than 0.78.

Despite the abundance of the literature related to the phenomenon, it is still difficult to compare experimental measurements of triple flame propagation with analytical or numerical results due to a lack of quantitative data in idealized configurations. Therefore, it is necessary to study the flame propagation phenomenon further and clarify how propagating triple flames transform into other structures in the vicinity of a burner.

Our objective in this context is to examine the characteristics of a propagating triple flame that is ignited downstream of a burner in the nonuniform mixture of an axisymmetric jet. The propagation speed of the flamefront in laboratory coordinates is measured using a high-speed camera. A comprehensive, time-dependent computational model is used to simulate the transient ignition and flame propagation phenomena under normal-gravity conditions. The model employs a detailed description of methane–air chemistry and transport properties. The numerical results are validated through a comparison with experimental measurements and then used to investigate the characteristics in the vicinity of the triple point of a propagating triple flame. In addition, the transition of a propagating triple flame into a double flame is examined by following the dominant reactions.

## 2. Experimental and numerical methods

### 2.1. Experimental method

The transient processes associated with ignition and flame propagation in methane–air mixtures were investigated using an annular concentric burner that is schematically presented in figure 1. The brass burner consists of a central tube with an inner diameter of 4.5 mm and an outer diameter of 6.1 mm, which is surrounded by a concentric outer tube of inner diameter 11.4 mm. The burner has a length of 200 mm to ensure fully developed Poiseuille flow at the exit. A hollow acrylic cylinder with a diameter of 120 mm was placed concentrically around the burner to minimize the effect of outside disturbances. Either methane or methane–air fuel-rich mixtures were introduced from the inner tube, while air was introduced from the outer tube.

The methane–air mixtures were ignited 35 mm downstream from the burner exit by a pulsed Nd:YAG laser (Continuum, Surelite SL II-10) with a maximum power of 300 mJ at 532 nm. The laser ignition system is shown schematically in figure 1. The laser beam was focused with a convex lens and the mixture was ignited at the focal point using a single shot with a duration of 6 ns. A successful ignition event was generally followed by the formation of a triple flame that propagated upstream and eventually stabilized at the burner exit. Flame propagation images were recorded by a high-speed video camera (Kodak EktaPro) with a 1 ms exposure time (at 1000 frames per second).

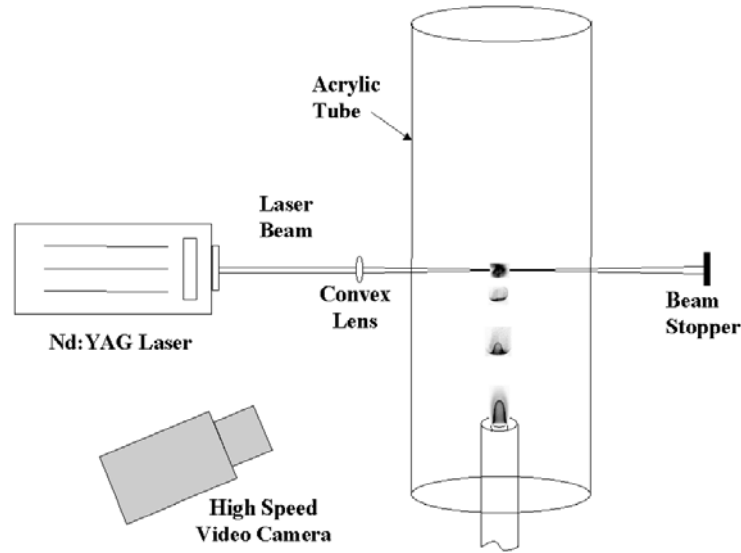


**Figure 1.** Schematic of the experimental set-up.

**Table 1.** Flame properties at the triple points for the three grid systems shown in figure 9.

Grid	301 × 101	451 × 125	601 × 201
$r$ (mm)	3.27	3.29	3.32
$z$ (mm)	16.21	16.26	16.24
$T$ (K)	1015	1055	1063
$q$ (kJ m <sup>-3</sup> s <sup>-1</sup> )	367	358	344
$V$ (m s <sup>-1</sup> )	0.28	0.36	0.39
Curvature (m <sup>-1</sup> )	256	438	562
$S_d$ (m s <sup>-1</sup> )	0.75	0.87	0.89
$V_{i,z}$ (m s <sup>-1</sup> )	0.46	0.51	0.56
$\kappa$ (s <sup>-1</sup> )	413	624	730
$\kappa_h$ (s <sup>-1</sup> )	147	172	176
$\kappa_c$ (s <sup>-1</sup> )	266	452	554

## 2.2. Numerical method

The numerical model is based on the solution of time-dependent governing equations for a two-dimensional reacting flow. Using cylindrical coordinates ( $r, z$ ), these equations can be written in the form

$$\frac{\partial(\rho\Phi)}{\partial t} + \frac{\partial(\rho v\Phi)}{\partial z} + \frac{\partial(\rho u\Phi)}{\partial r} = \frac{\partial}{\partial z} \left( \Gamma^\Phi \frac{\partial\Phi}{\partial z} \right) + \frac{\partial}{\partial r} \left( \Gamma^\Phi \frac{\partial\Phi}{\partial r} \right) - \frac{\rho u\Phi}{r} + \frac{\Gamma^\Phi}{r} \frac{\partial\Phi}{\partial r} + S^\Phi, \quad (1)$$

where  $\rho$  is the density, and  $u$  and  $v$  represent the radial ( $r$ ) and axial ( $z$ ) velocity components, respectively. The general form of the equation represents either of the mass, momentum, species, or energy conservation equations, depending on the variable used in the place of  $\Phi$ . The gravitational acceleration term is included in the axial momentum equation. The transport coefficient  $\Gamma^\Phi$  and the source terms  $S^\Phi$  appearing in the governing equations are provided in table 1 of [19].

Using the optically thin assumption, thermal radiation heat loss is modelled by adding a sink term to the energy equation. According to this approximation, the radiation heat loss,  $q_{\text{rad}}$ , is [20]

$$q_{\text{rad}} = -4\sigma K_{\text{p}}(T^4 - T_0^4), \quad (2)$$

where  $\sigma$  denotes the Stefan–Boltzmann constant, and  $T$  and  $T_0$  the local flame and ambient temperature, respectively. The Planck mean absorption coefficient  $K_{\text{p}}$  accounts for the absorption and emission from the participating gaseous species  $\text{CO}_2$ ,  $\text{H}_2\text{O}$ ,  $\text{CO}$  and  $\text{CH}_4$ , and is expressed as

$$K_{\text{p}} = P \sum_k x_k K_{\text{p},k}, \quad (3)$$

where  $P$  denotes the pressure,  $x_k$  the mole fraction of species  $k$ , and  $K_{\text{p},k}$  the mean absorption coefficient of that species. The value of  $K_{\text{p},k}$  is obtained by using a polynomial approximation to the experimental data provided in [21]. In normal gravity, the effect of radiation heat loss on the partially premixed flame structure is insignificant. For example, a double flame with an equivalence ratio of 2.5 and an inner flow velocity of  $0.3 \text{ m s}^{-1}$  has a maximum flame temperature of 1974 K when considering radiation and 2028 K when it is neglected. Detailed studies on the effects of gravity, radiation and co-flow on partially premixed flames are outside the scope of this paper, and can be found elsewhere [22].

The set of governing equations is completed by introducing the global species conservation equation and the state equation. The thermodynamic and transport properties appearing in the above equations are considered to be temperature and species dependent. First, the viscosity and thermal conductivity of the individual species are estimated based on the Chapman–Enskog collision theory, following which those of the mixture are determined using the Wilke semi-empirical formulae [23]. The Chapman–Enskog theory and the Lennard–Jones potentials are used to estimate the binary-diffusion coefficient between each species and nitrogen. A relatively detailed 24-species, 81-step mechanism involving both  $C_1$ - and  $C_2$ -containing species is used to represent the  $\text{CH}_4$ –air chemistry [24]. The mechanism has been validated for the computation of premixed flame speeds and the structure of NP and partially premixed flames [25, 26].

The computational domain is bounded by the symmetry plane and an outflow boundary in the radial direction, and by the inflow and another outflow boundary in the axial direction. Symmetric conditions are applied at the left boundary, whereas the right boundary is treated as a free surface. At the inflow boundary, a fully developed pipe flow in the inner tube and flat-velocity profiles outside the inner tube are used. For the inner wall, no-slip boundary condition is imposed. The temperature and species mass fraction profiles are assumed to be uniform at the inflow boundary. The flow variables at the axial outflow boundary are obtained using an extrapolation procedure with weighted zero- and first-order terms. The main criterion used in selecting the weighting functions is that the flow should exit the outflow boundary without being distorted. In addition, the outflow boundaries in both directions are located sufficiently far from the respective inflow and symmetric boundaries such that the propagation of boundary-induced disturbances is minimized. The dimensions of the computational domain and the boundary conditions are indicated in figure 2.

The computational model is based on an algorithm developed by Katta *et al* [27]. An implicit algorithm is employed to solve the unsteady gas-phase equations. The governing equations are integrated by using a ‘finite control volume’ approach with a staggered, nonuniform  $601 \times 201$  (axial  $\times$  radial-direction) grid system, which is shown in figure 3. Grid lines are clustered near the flame surfaces to resolve the steep gradients of the dependent variables. The minimum grid spacing is 0.06 mm in the  $r$ -direction and 0.065 mm in the

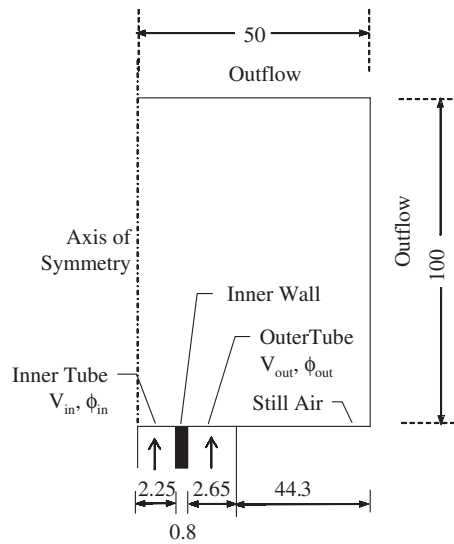


**Figure 2.** Schematic of the computational domain and boundary conditions. All dimensions are in millimetres.

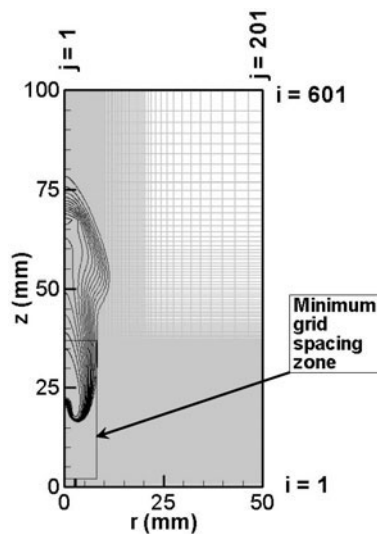


**Figure 3.** Computational grid used in the simulation. The small rectangle shows the minimum grid spacing region where the propagating flamefront is located.

$z$ -direction. The minimum values are located at the bottom-left corner of the domain. The isotherms of an instant propagating flame are superimposed on the mesh showing that the flamefront locates in the minimum grid spacing zone. The effect of grid size on flame propagation will be further discussed in the following section. An iterative ADI (alternating direction implicit) technique is used for solving the resulting  $(N_S+3)$  sets of algebraic equations. A stable numerical-integration procedure is achieved by coupling the species and energy equations through the chemical-reaction source terms. At every time step, the pressure field

is calculated by solving the pressure Poisson equations at all grid points simultaneously and utilizing the LU (lower and upper diagonal) matrix-decomposition technique.

### 2.3. Data analysis

Here, we calculate the local flame propagation speed,  $S_d$ , flame stretch rate,  $\kappa$ , and flamefront curvature from the simulations. The determination of curvature and stretch in multi-dimensional configurations requires (i) the identification of a flame surface and (ii) an application of analytical expressions for stretch and curvature to that surface. For flamefront tracking models in turbulent combustion, the relevant flame speed is the flame propagation speed  $S_d$ , which is defined as the normal flamefront velocity with respect to local gas velocity.

The flame surface is identified as a uniform surface of a transported scalar  $\varphi$ . The governing transport equation for  $\varphi$  is

$$\frac{\partial \varphi}{\partial t} + \mathbf{V}_{\text{fluid}} \cdot \nabla \varphi = \frac{1}{\rho} \nabla \cdot (\rho D \nabla \varphi) + \frac{\omega_\varphi}{\rho}, \quad (4)$$

where  $\mathbf{V}_{\text{fluid}}$  is the gas velocity at the surface,  $D$  the diffusion coefficient for the scalar and  $\omega_\varphi$  is the volumetric rate of generation or destruction of the scalar. The propagation velocity of the flame surface contour in the laboratory coordinate,  $\mathbf{V}_f$ , is the sum of the convective component and its propagation relative to the gas

$$\mathbf{V}_f = \mathbf{V}_{\text{fluid}} + S_d \mathbf{n}, \quad (5)$$

where  $\mathbf{n}$  is the unit normal vector of the contour of  $\varphi$  directed towards the unburnt gas, and can be expressed as

$$\mathbf{n} = \pm \frac{\nabla \varphi}{|\nabla \varphi|}, \quad (6)$$

where the sign is positive for reactants and negative for products, such that  $\mathbf{n}$  is always directed towards the direction of flame propagation. On the flame surface, i.e. the contour of  $\varphi$ , we have

$$\frac{d\varphi}{dt} = \frac{\partial \varphi}{\partial t} + \mathbf{V}_f \cdot \nabla \varphi = 0. \quad (7)$$

Substituting equations (4) into (7), the flame propagation speed can be expressed as

$$S_d = \mp \frac{1}{\rho |\nabla \varphi|} [\nabla \cdot (\rho D \nabla \varphi) + \omega_\varphi], \quad (8)$$

where the sign is negative for reactants and positive for products.

Following the methodology of Chung and Law [28], assuming that the tangential component of the flame surface velocity is equal to the tangential component of the local fluid velocity, the flame stretch may be expressed in the form

$$\kappa = \nabla \cdot \mathbf{V}_{\text{fluid},t} + (\mathbf{V}_f \cdot \mathbf{n})(\nabla \cdot \mathbf{n}). \quad (9)$$

The term  $\nabla \cdot \mathbf{n}$  represents the curvature of the flamefront. The subscript 't' denotes the tangential component of the velocity. Algebraic manipulation using standard identities of vector and tensor calculus yields the following expression for the flame stretch:

$$\kappa = \nabla \cdot \mathbf{V}_{\text{fluid}} - \mathbf{nn} : \nabla \mathbf{V}_{\text{fluid}} + [(\mathbf{V}_f - \mathbf{V}_{\text{fluid}}) \cdot \mathbf{n}](\nabla \cdot \mathbf{n}). \quad (10)$$

Using the definition of flame propagation speed, one can finally express the flame stretch in the form

$$\kappa = \nabla \cdot \mathbf{V}_{\text{fluid}} - \mathbf{nn} : \nabla \mathbf{V}_{\text{fluid}} + S_d (\nabla \cdot \mathbf{n}), \quad (11)$$



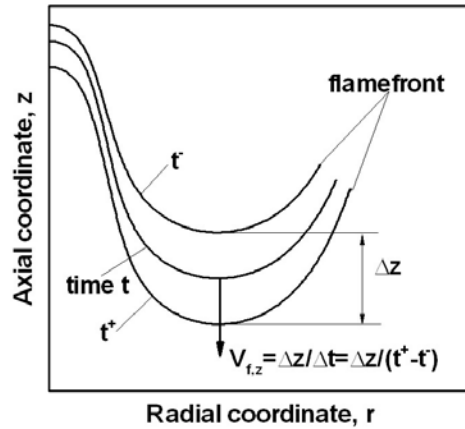


**Figure 4.** Illustration showing the experimental determination of the axial component of the propagation velocity of the flamefront in laboratory coordinates. The times  $t^+$  and  $t^-$  occur just after and prior to time  $t$  and have different corresponding flamefront locations.

which is identical to that obtained by Candel and Poinot [29] and Zhong *et al* [30]. In equation (11), the first two terms represent the tangential component of the rate of strain and are called hydrodynamic stretch ( $\kappa_h$ ). The last term accounts for the curvature effect and is called curvature stretch ( $\kappa_c$ ). In equations (10) and (11), the term  $\mathbf{nn} : \nabla \mathbf{V}_{\text{fluid}}$  refers to the double-dot (scalar) product between the dyads  $\mathbf{nn}$  and  $\nabla \mathbf{V}_{\text{fluid}}$ , i.e.

$$\mathbf{nn} : \nabla \mathbf{V}_{\text{fluid}} = \sum_i \sum_j n_i n_j \frac{\partial V_i}{\partial x_j}. \quad (12)$$

The axial component of the propagation velocity of the flamefront in the laboratory coordinate can be experimentally measured from the images obtained by the high-speed video camera so that

$$V_{f,z} = \frac{\Delta z}{\Delta t}, \quad (13)$$

where the subscript 'z' denotes the axial component of the velocity,  $\Delta z$  the distance between two sequential flame images along the axial direction at the flame base, and  $\Delta t$  the time difference. Figure 4 schematically illustrates the experimental determination of  $V_{f,z}$  at an instant of time  $t$ , where the average value between the adjacent time  $t^+$  and  $t^-$  is used. On the other hand, according to equation (3),  $V_{f,z}$  can also be obtained from numerical results by using the relation

$$V_{f,z} = V_{\text{fluid},z} + S_d n_z, \quad (14)$$

where  $n_z$  is the axial component of the unit normal vector of the contour of  $\varphi$ .

#### 2.4. Determination of triple points

There is some latitude regarding the choice of an appropriate transported scalar  $\varphi$  that represents the flamefront. Najm and Wyckoff [31] and De Goey *et al* [32] used a particular value of the fuel mass fraction to identify the flame surface. Im and Chen [33] used a specific mass fraction contour of a product species ( $\text{H}_2\text{O}$ ) to identify the reaction zone of partially premixed  $\text{H}_2$ -air mixtures. We have shown that the OH contour clearly identifies the RP and LP reaction zones

of lifted triple flames [34], and that representation is employed herein. An OH mass fraction of  $3.5 \times 10^{-5}$  satisfactorily locates the flame surface in the context of our investigation.

The triple point at the flame base is defined as the location of the intersection of the stoichiometric mixture fraction line and the specified OH contour. The definition of mixture fraction follows that of Bilger [35], i.e.

$$\xi = \frac{2Z_C/W_C + (1/2)Z_H/W_H + (Z_{O,2} - Z_O)/W_O}{2Z_{C,1}/W_C + (1/2)Z_{H,1}/W_H + Z_{O,2}/W_O}, \quad (15)$$

where  $Z_i$  denotes the mass fraction of the element  $i$  of atomic mass  $W_i$ , the subscripts C, H and O refer to carbon, hydrogen, and oxygen, and the subscripts 1 and 2 refer to the fuel and oxidant reference states. The mixture fraction definition of equation (15) is generally employed to investigate NP flames, but we have previously shown that mixture-fraction-based state relationships can also be developed for partially premixed flames [36, 37]. We have employed detailed simulations and equation (15) is applied based on the 'exact' concentration field. The application of the mixture fraction is based on an implicit assumption of unit Lewis number.

### 3. Results and discussion

#### 3.1. Ignition and flame propagation

A methane–air mixture at an equivalence ratio of 2.0 and with a mean burner exit velocity  $V = 0.5 \text{ m s}^{-1}$  was introduced from the inner tube, and an air stream with a mean velocity of  $0.3 \text{ m s}^{-1}$  was supplied from the outer tube. The observations from this configuration allowed us to examine the formation and propagation of a triple flame in a partially premixed jet. The value of the stoichiometric mixture fraction  $\xi_{st}$  obtained using equation (15) for this case is 0.375. The Reynolds number ( $Re_d = Vd/\nu$ ) of the inner jet is roughly 225, where  $d$  is the inner tube diameter and  $\nu$  the kinematic viscosity of methane–air mixture.

Methane–air mixtures were ignited at a 35 mm height downstream of the burner exit. Figure 5 presents the temporal evolution of the flame topology in the form of high-speed video images. The images were post-processed by L View Pro Image software. The images begin with flame ignition and subsequently show the flame propagating to a stationary burner-stabilized state. In general, two reacting volumes (or kernels) are formed following ignition. One propagates downstream and is quickly extinguished. The other propagates upstream towards the burner and develops into a triple flame, which is the focus of this investigation. The triple point is clearly established by  $t \approx 5 \text{ ms}$  and a well-defined triple flame develops at  $\approx 12 \text{ ms}$ . The RP and LP reaction zones, as well as the NP reaction zone that is located between the RP and LP reaction zones, can be readily identified in the 12 and 24 ms images. As the flame propagates upstream, the inner RP and the NP reaction zones become longer, and globally they both appear to move more slowly than the triple point or leading edge of the flame. Simultaneously, the flame curvature around the triple point increases significantly. When the triple flame approaches the burner and is stabilized near its exit, it transforms into a double flame due to the absence of the mixing layer; i.e. the outer LP reaction zone loses its distinct identity and merges with the NP reaction zone.

Figure 6 presents the simulated results of transient ignition and flame propagation processes, which are represented through the heat release rate contours for the same incremental times corresponding to figure 5. To ignite the mixture, a rectangular zone of area  $2 \text{ mm}^2$  centred at  $z = 35 \text{ mm}$  was set to an initial temperature of 1800 K. Also, the radical H and O mass fractions were set to 0.005 in this zone. After a short period (i.e. less than 0.1 ms), these conditions were removed and the flame developed by itself. The transient processes

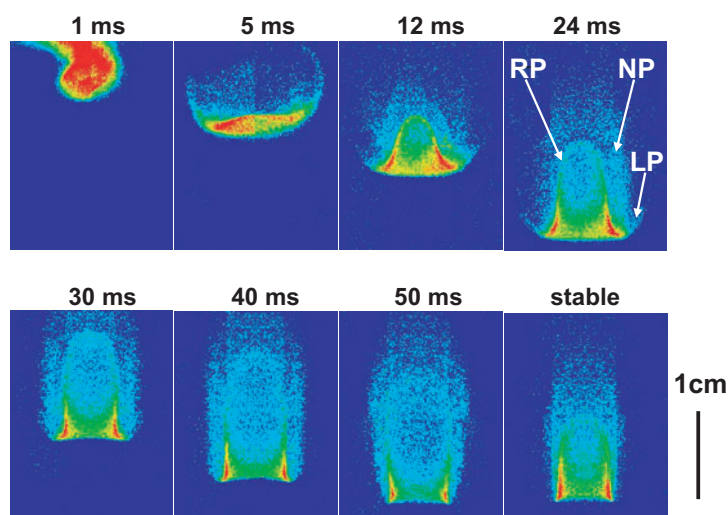


**Figure 5.** High-speed video camera images showing the temporal evolution of ignition and flame propagation. The methane–air mixture of an equivalence ratio  $\Phi = 2$  and a mean velocity of  $V_{\text{in}} = 0.5 \text{ m s}^{-1}$  is introduced from the inner tube, and air at a mean velocity of  $V_{\text{out}} = 0.3 \text{ m s}^{-1}$  from the outer tube. The notation RP, NP, and LP is used to represent the RP, NP, and LP reaction zones, respectively.


associated with the formation of a reacting volume, its evolution into a triple flame followed by the upstream propagation of the triple flame, and its stabilization near the burner rim in the form of a double flame are clearly reproduced by the simulation. Comparing figures 5 and 6, we observe that despite some differences in the flame topology, the simulated results are in good agreement with the experimental observations with respect to the position of the propagating flame, the flame height and width, and the final shape of the burner-stabilized flame. The heat release rates at the flame base (or around the triple point) decrease as the flame approaches the burner, which can be confirmed from the luminescence intensity in figure 5. This is due to the fact that, as the flame moves further upstream, the mixing layer thickness becomes smaller. Consequently, the burning around the flame base is less premixed-like and has diminished chemical reactivity.

### 3.2. Effect of grid size on flame propagation

We calculated the laminar burning velocity of a stoichiometric methane–air freely propagating flame using the Sandia PREMIX code [38] with the  $\text{C}_2$  reaction mechanism employed in the simulation. The flame speed of a planar flame  $S_{\text{L}0}$  monotonically converges from  $0.44 \text{ m s}^{-1}$  using 39 grid points to a constant value of  $0.40 \text{ m s}^{-1}$  when 941 points are used. The latter result is in agreement with the literature [39]. Figure 7 presents a comparison of the mass fractions of  $\text{CH}_4$ ,  $\text{O}_2$ , and  $\text{OH}$ , and the temperature and axial velocity obtained from the PREMIX code with those resulting from the axisymmetric simulation (along an axial traverse) at an arbitrary time. The thick dark line in the inset in figure 7(a) shows the location where the data are recorded across the triple point of the propagating flame. The solid lines represent the data from the PREMIX code, and the dashed lines correspond to results from the propagating flame simulation. The origins of both datasets are placed at  $T = 300 \text{ K}$ . The centre of the PREMIX flame simulation lies at  $1 \text{ mm}$  and the associated flame thickness is roughly  $0.5 \text{ mm}$ .

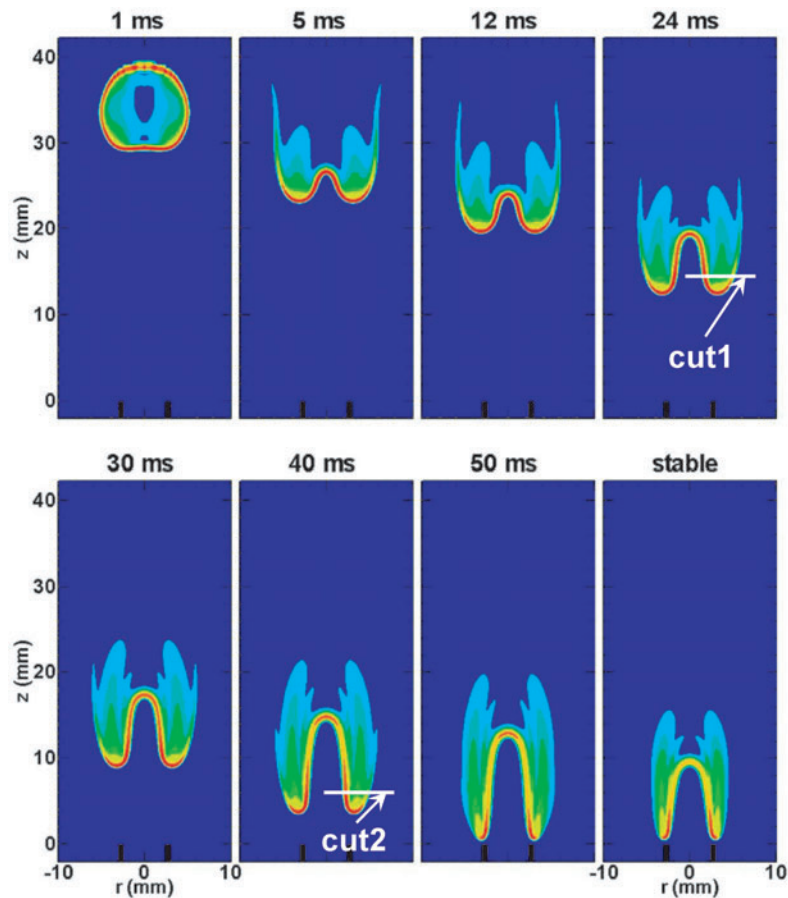


**Figure 6.** Simulated results showing the temporal evolution of ignition and flame propagation in terms of heat release rate contours. Each image contains ten contours beginning from a value of  $50 \text{ kJ m}^{-3} \text{ s}^{-1}$  with successive  $100 \text{ kJ m}^{-3} \text{ s}^{-1}$  intervals.

 An animated GIF of this figure is available from [stacks.iop.org/CTM/8/293](https://stacks.iop.org/CTM/8/293)

The mass fraction profiles of methane, oxygen, and OH exhibit similar trends for both the configurations, showing that the flame structure in the vicinity of the triple point is similar to that of a premixed flame. The flame thickness of the triple flame is roughly 1 mm, but the peak temperature is lower since the highest temperatures in the axisymmetric flame are located along its centreline. The axial velocity ahead of the triple point decreases to a small negative value due to flow expansion and divergence, consistent with the results of Ruetsch *et al* [9]. Since the two configurations are different, it is particularly interesting that near the triple flame base, its structure closely resembles that of the simpler one-dimensional planar flame.

We have previously reported measurements pertaining to burner-stabilized [40] and lifted [34] methane–air partially premixed triple flames, including those of chemiluminescence emission, temperature (using holographic interferometry), and velocity (using particle image velocimetry). This permitted a detailed validation of our numerical model, which compared the measured and predicted velocity and temperature fields, the experimentally obtained  $\text{C}_2^*$  chemiluminescent emission with predicted volumetric heat release rates, the measured and

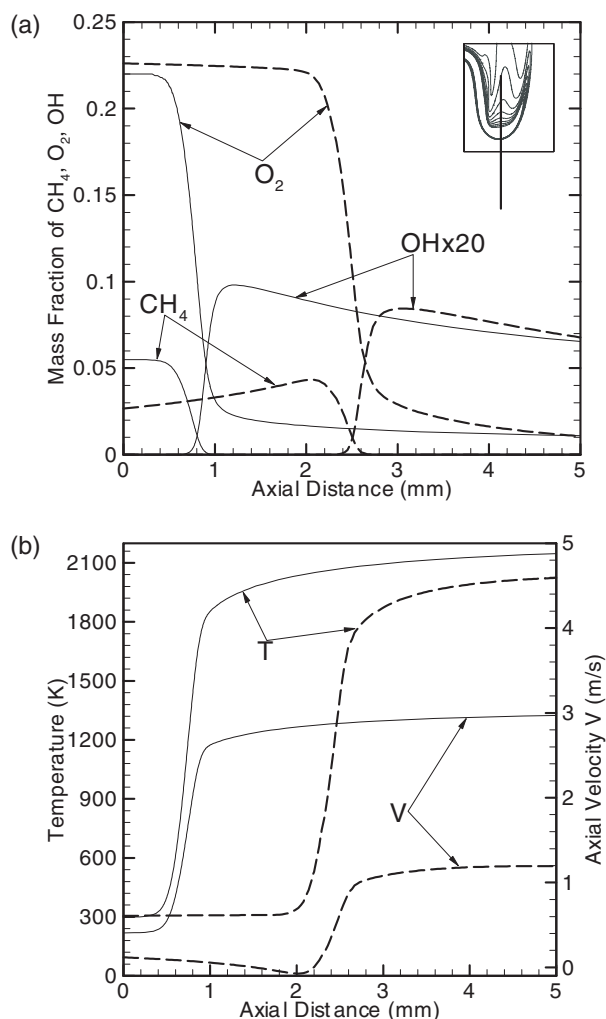


**Figure 7.** Comparison of the profiles of  $\text{CH}_4$ ,  $\text{O}_2$ , and  $\text{OH}$  mass fraction, temperature and axial velocity between a simulated one-dimensional stoichiometric planar flame (—) and along an axial traverse for an axisymmetric propagating triple flame. The inset in (a) shows the location of the cut that crosses the triple point.

predicted flickering frequencies, and unsteady reaction zone topologies. Here, we characterize grid effects on simulations of flame propagation.

Figure 8 presents the evolution of a temperature contour of 1000 K at three time steps for four different grids, i.e.  $301 \times 101$ ,  $451 \times 125$ ,  $591 \times 151$ , and  $601 \times 201$  (in the axial  $\times$  radial-direction). For all four grids, the calculation begins at 1 ms using the same initial restart file of grid  $301 \times 101$ . The interpolation procedure employed in the code for different grid spacings has no effect on the simulation, as can be seen from the fact that all of the isotherms collapse on to each other at 1.1 ms. However, as the flame propagates further upstream, the isotherms moved at different speeds for the four grids, with the finest  $601 \times 201$  grid corresponding to the maximum propagation velocity. The differences between the results for grids  $591 \times 151$  and  $601 \times 201$  are small, suggesting the convergence of the flame propagation velocity.

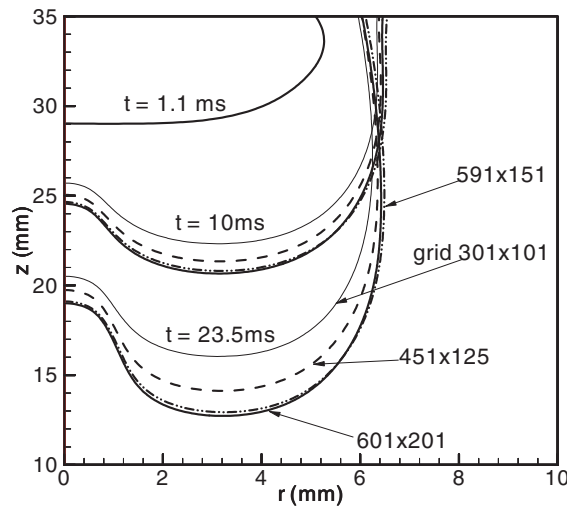


**Figure 8.** Evolution of a temperature contour of 1000 K for four different grids at three time steps. The thin solid line represents a  $301 \times 101$  grid; dashed line,  $451 \times 125$  grid; dash-dot line,  $591 \times 151$  grid; and thick solid line,  $601 \times 201$  grid. For all cases, the flame is restarted from a profile obtained for 1 ms for a  $301 \times 101$  grid.

Increasing the grid resolution for a partially premixed flame also changes the local mixing and scalar gradients and, therefore, the chemical kinetics (assuming that a coarser grid has a poorer resolution of the local gradients). The convergence path for the propagation velocity depends on the scheme employed in the code and does not necessarily begin from a higher value as shown in the PREMIX code results. In the axisymmetric simulation, the propagation velocity has a smaller value for larger grid spacing, and converges to a larger value as the grid resolution improves. For methane–air mixtures, the grid spacing should be smaller than 0.05 mm so that the flame thickness can be represented by at least 20 grid points to obtain reasonable grid-independent flame propagation. A uniform high-resolution grid is preferable to accurately track the evolution of the entire flame over time. However, to represent the experimental configuration in this manner requires more than two million grid points, which is virtually impossible based on current computer resources for simulations that use detailed chemistry. We conclude from the convergent behaviour presented in figure 8 that the finest grid system we are using for the flame propagation speed study is adequate.

Figure 9 presents OH contours (solid lines) that represent the instantaneous flamefront location near an axial location of 16.2 mm for three grids. The dashed line denotes the stoichiometric mixture fraction  $\xi_{st}$  contour. The times when the flamefronts reach this location are 26.5 ms, 23.0 ms, and 20.5 ms, respectively, for the  $301 \times 101$ ,  $451 \times 125$ , and  $601 \times 201$  grids. Table 1 lists the flame properties at the triple points that are represented by the intersection of the OH and  $\xi_{st}$  contours. Although the  $301 \times 101$  grid has nearly four times less points than for the  $601 \times 201$  simulation, the flamefront shapes (or the triple point positions) near the 16.2 mm location are nearly identical except in the far downstream region. The flame temperature and heat release rates at the respective triple points are also nearly the same.

However, as shown in table 1, the flame dynamics is dissimilar for the three grids. As the resolution increases, the simulated flamefront becomes smoother and is more geometrically continuous, which results in smaller flame radii. The higher flame propagation speed is attributed to larger heat and mass fluxes. As the flame propagation speed increases, these

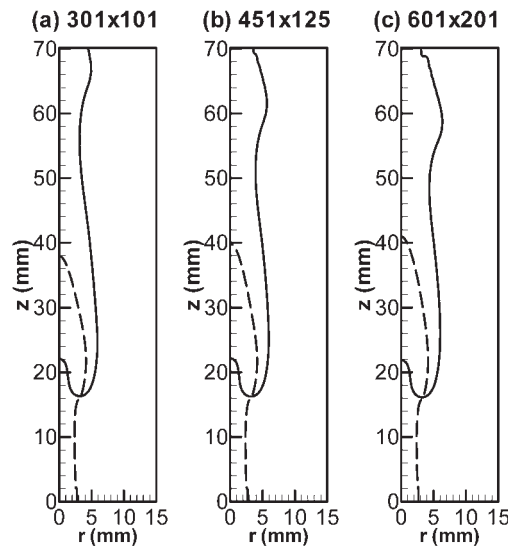


**Figure 9.** OH contour (—) that represents the instantaneous flamefront location near an axial location of 16.2 mm for three grids. The dashed line denotes the stoichiometric mixture fraction  $\xi_{st}$  contour.

fluxes are determined by increasing the number of grid points (or decreasing the grid spacing) in the region between the unburned gas and the thin flame. We observe from figure 9 that the normal to the flamefront at the triple point is nearly parallel to the axial-direction, i.e.  $n_z \approx n = 1$ . The flame propagation speed equals the sum of the axial flow velocity and the axial flamefront propagation velocity in laboratory coordinates, as represented by equation (9). From table 1, it is seen that for all three grids, the curvature-induced stretch is much larger than the hydrodynamic stretch. This will be further discussed in a later section. In the following, we use the simulation results of grid  $601 \times 201$  to further analyse the flame dynamics at the triple points of the propagating flame.

### 3.3. Flame dynamics at the triple point

Figure 10 presents the flame propagation speed ( $S_d$ ) and the axial flamefront propagation velocity ( $V_{f,z}$ ) in laboratory coordinates at the triple points that are defined in the previous section. The data are inferred from the simulations with respect to axial displacement. The experimentally obtained values of  $V_{f,z}$  from high-speed video images are through the application of equation (13). The flame speeds are normalized by the laminar burning velocity  $S_{L0}$  ( $=0.40 \text{ m s}^{-1}$ ) of a stoichiometric methane–air mixture [39]. Both predicted and measured values of  $V_{f,z}$  remain nearly constant at locations above  $z = 8 \text{ mm}$ , but decrease rapidly when the flame propagates lower than 8 mm. The flame propagation speed decreases linearly and monotonically as the flame propagates upstream. The value of  $S_d$  is much larger than that of  $S_{L0}$ , which is in accord with Ko and Chung’s measurements [17] and the predictions of Hartley *et al* [8] and Ruetsch *et al* [9]. The investigation of Ko and Chung [17] focused on the far field region ( $20 \text{ mm} < z < 200 \text{ mm}$ ), while this investigation considers flame propagation in the near jet region closer to the burner rim where burner re-attachment issues are important. Moreover, there is good agreement between the measured and predicted flame speeds, except for a small discrepancy near the burner rim.

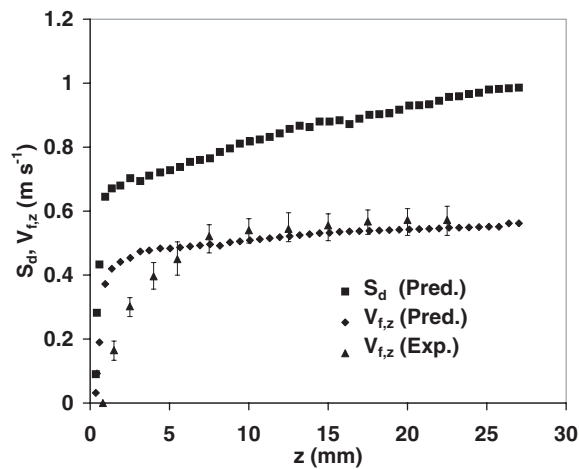


**Figure 10.** Predicted flame propagation speed and axial flamefront propagation velocity at the triple points. The experimentally obtained values of  $V_{f,z}$  from high-speed video images by applying equation (13) are also presented.

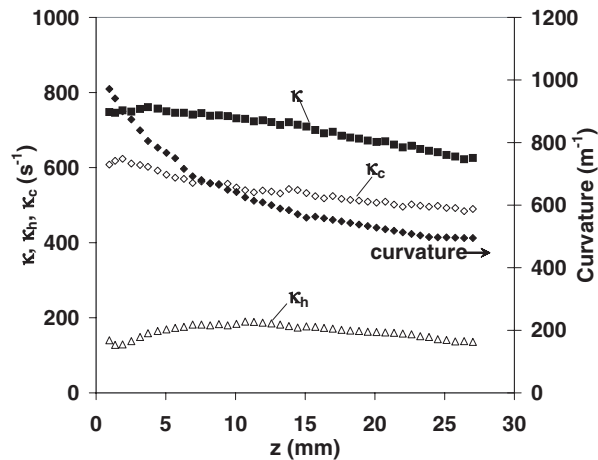


**Figure 11.** Flame curvature and stretch rate (including the hydrodynamic stretch  $\kappa_h$ , curvature stretch  $\kappa_c$  and total stretch rate  $\kappa$ ) at the triple point of the propagating flame.

The curvature and total stretch rate (characterized by the hydrodynamic stretch  $\kappa_h$  and the curvature induced stretch  $\kappa_c$ , where  $\kappa = \kappa_h + \kappa_c$ ) at the triple point of the propagating flame are presented in figure 11 as a function of the triple point location. As the flame approaches the burner, the curvature at the flamefront increases to as much as twice its downstream value. We infer from figures 10 and 11 that a uniform correlation exists between the flame propagation speed and the flame curvature. The propagation speed decreases with increasing positive flame curvature due to flow redirection. During the flame propagation process, the hydrodynamic stretch remains nearly constant and slightly decreases near the burner wall. The value of  $\kappa_h$  is much lower than that of  $\kappa_c$ , which is three times larger than  $\kappa_h$ . These results show that curvature-induced stretch dominates over the hydrodynamic stretch during the triple flame propagation. The total stretch rate increases from  $630$  to  $780$   $s^{-1}$ . These values are much



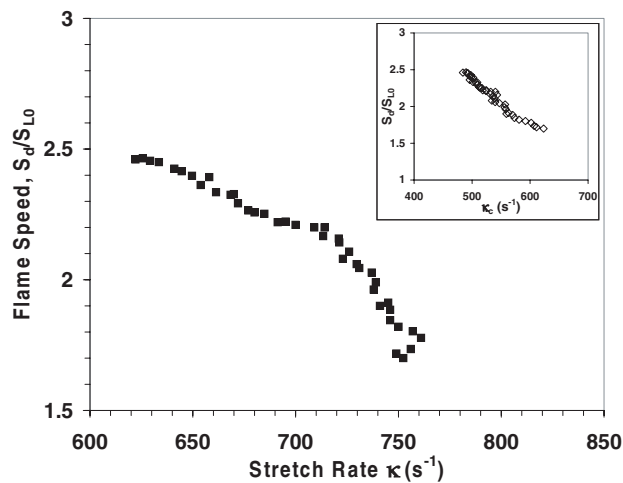


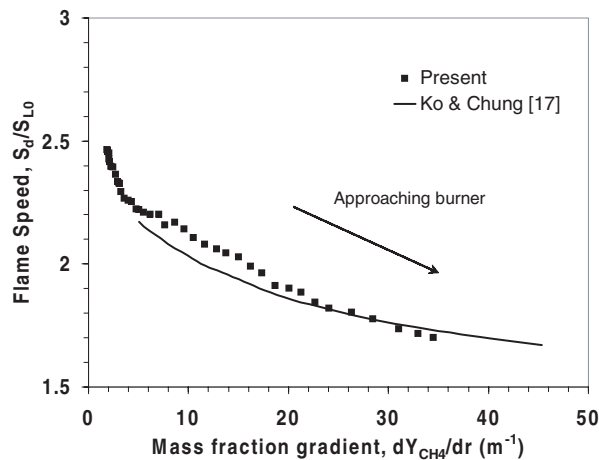
**Figure 12.** Relationship between the flame propagation speed and flame stretch rate.

larger than those reported by Ko and Chung [17], whose values ranged between 300 and  $450 \text{ s}^{-1}$  for a jet with  $Re_d = 214$  ( $Re_d = 225$  for the flame that we are discussing).

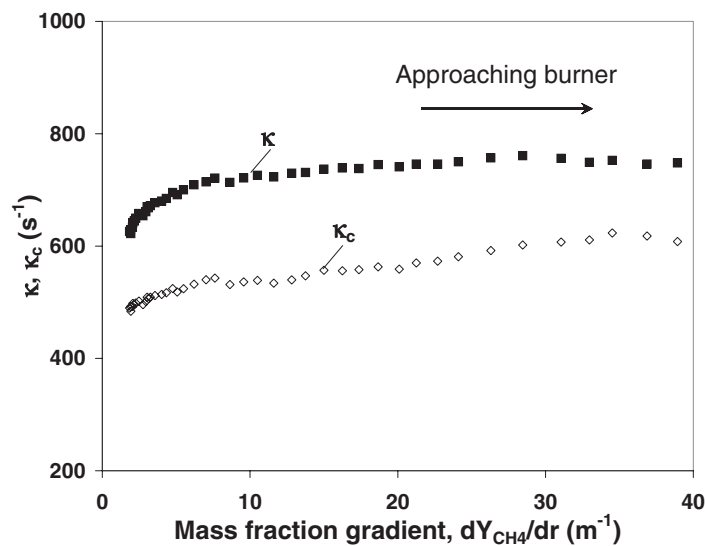
A propagating flame can be influenced by both flame stretch and differential diffusion. We calculated the Lewis numbers,  $Le = \lambda/(\rho D_{k-N_2} c_p)$ , where  $\lambda$  and  $c_p$  are the thermal conductivity and specific heat of the mixture, respectively, and  $D_{k-N_2}$  is the binary-diffusion coefficient of the  $k$ th species to nitrogen, with the  $k$ th species being methane or oxygen at the various triple points. During flame propagation, the values of  $Le$  are  $\sim 0.93$  for methane and  $\sim 1.02$  for oxygen, with these values remaining virtually unchanged. Therefore, the effective Lewis number at the triple points is nearly unity and, consequently, the influence of differential diffusion on the flame structure is small.

Figure 12 presents the response of the flame propagation speed to the total flame stretch at the triple point. The inset shows the flame speed response to the curvature induced flame stretch. Data are plotted only in the range of  $2 \text{ mm} < z < 30 \text{ mm}$ , since near the burner the flamefront interacts with the burner rim making for a more complex heat and mass transfer scenario, which is challenging to model. The flame speed decreases with increasing stretch rate, with this decrease becoming more rapid near the burner exit. The curvature induced flame stretch exhibits a linear correlation with flame speed. As the flame propagates upstream and the radius of curvature becomes smaller, the stretch due to curvature for the positively curved and convex flame becomes dominant. Since positive curvature induces a positive stretch rate, this decreases the flame propagation speed by lowering the local reaction and heat generation rates [41]. In figure 12, there appear to be two distinct regions, characterized by two distinct slopes and it is hypothesized that the sudden change in the slope corresponds to the transition from the triple to the double flame structure.

Figure 13 presents the relationship between the flame propagation speed and fuel mass fraction gradient ( $dY_{CH_4}/dr$ ). It is seen that the fuel mass fraction increases as the flame approaches the burner. As the flame propagates upstream, the flame speed decreases almost linearly as this gradient increases. This behaviour is consistent with the previous experimental and computational studies [9, 17]. As discussed by Ruetsch *et al* [9], the change in fuel fraction gradient modifies the burning that occurs in the premixed and NP regions near the triple points. When the mixture fraction gradient is small, the burning is more premixed-like and the triple



**Figure 13.** Relationship between the flame propagation speed and fuel mass fraction gradient at the triple points. The result of Ko and Chung [17] is the curve-fitted data.



**Figure 14.** Variation of curvature-induced and total stretch rate with respect to the mass fraction gradient.

flame is broader with a smaller curvature around the triple point. In this case, the flame speed increases as a result of the increase in flow redirection. On the other hand, for a larger mixture fraction gradient, the burning is more NP-like with a smaller increase in the flame speed.

In the present investigation, we hypothesize that as the flame propagates upstream, the increase in mass fraction gradient causes an increase in the flame curvature near the triple point. This increases the curvature induced stretch, since the hydrodynamic induced stretch is relatively small, which in turn reduces the flame speed, as discussed in the context of figure 12. The variation of the curvature-induced stretch and the total stretch with respect to the mass fraction gradient is presented in figure 14, and supports this hypothesis.

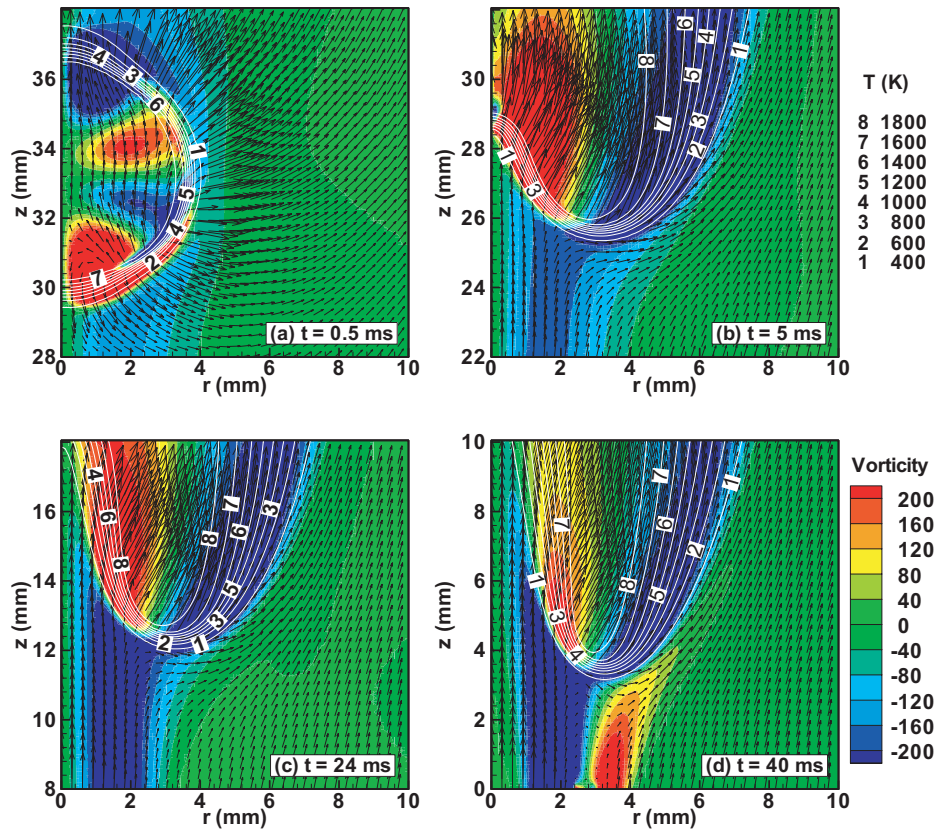


**Figure 15.** Simulated vorticity contours, temperature contours (white lines) and velocity vectors showing the vorticity evolution at four different times during triple flame development and propagation.

### 3.4. Flowfield near the flamefront

During the ignition and flame propagation process, the flowfield ahead of the flamefront is worth investigating, since it influences the flamefront dynamics. This transient process is difficult to observe experimentally, for example, by particle-tracking velocimetry, due to the small timescales involved. Therefore, numerical simulations can provide further insight into this problem. Figure 15 presents the instantaneous vorticity contours, isotherms and velocity vector plots at four different times during the development and propagation of the triple flame. Figure 15(a) presents the flame development process just following ignition, figures 15(b) and (c) the triple flame propagation, and figure 15(d) a double flame that is formed during the process of stabilization near the burner wall. A vortex is established following ignition at  $(z, r) \approx (30.0 \text{ mm}, 1.0 \text{ mm})$ , i.e. in the lower portion of the ignition kernel or reacting volume (cf figure 15(a)). The ignition kernel subsequently develops into a triple flame and the vortex is dissipated as this flame propagates upstream, which is shown in figures 15(b) and (c). We can observe from figure 15 that as the flame proceeds into the unburned gases it behaves much like a solid body travelling against the incoming flow. In general, the volumetric expansion resulting from a stationary flame generates a positive pressure gradient for the incoming reactant flow, which, in turn, decelerates and/or deflects the fluid entering the flame zone. The velocity of

a stretched propagating flame is higher than that of a corresponding unstretched stationary flame. The higher burning velocity causes stronger volumetric expansion and generates larger pressure gradients in the incoming flow. When the flow velocity is small, this large pressure gradient causes flow reversal in the upstream region of the flame edge as seen in figure 15. However, as the flame becomes stationary when it reaches the burner tip, a decrease in the flow velocity occurs in the region upstream of the flame edge.

Figures 15(b) and (d) also indicate regions of large positive and negative vorticity near the RP and LP zones, respectively. This vorticity is generated by flow expansion or dilatation due to heat release in the two reaction zones. As the flame approaches the burner and the LP reaction zone merges with the NP reaction zone, the positive vorticity field interacts with the vorticity field generated at the burner wall. A small recirculation zone is established downstream of the wall that aids in the flame stabilization process (cf figure 15(d)) as the double flame stabilizes near the burner wall.

### 3.5. Transition from a triple flame to a double flame

As the flame approaches the burner wall, the mixture fraction gradient increases (or the mixing length decreases) and the LP wing of the triple flame diminishes in size and merges with the NP wing to form a double (partially premixed) flame near the burner rim. We can gain further understanding of these phenomena by examining the dominant reaction pathway during this transition from a triple flame to a double flame. The instantaneous images of the heat release rate contours discussed in the context of figure 6 indicated that during the transition, which occurs around  $z \approx 5\text{--}8$  mm, the propagating flame loses its LP wing due to local extinction.

The simulations were used to identify the following six dominant reactions during this transition:

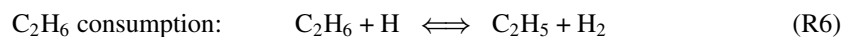
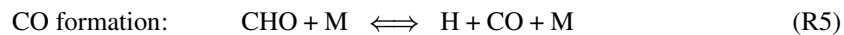
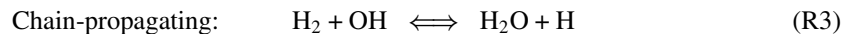
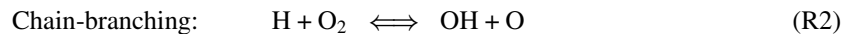
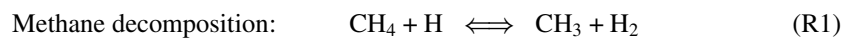
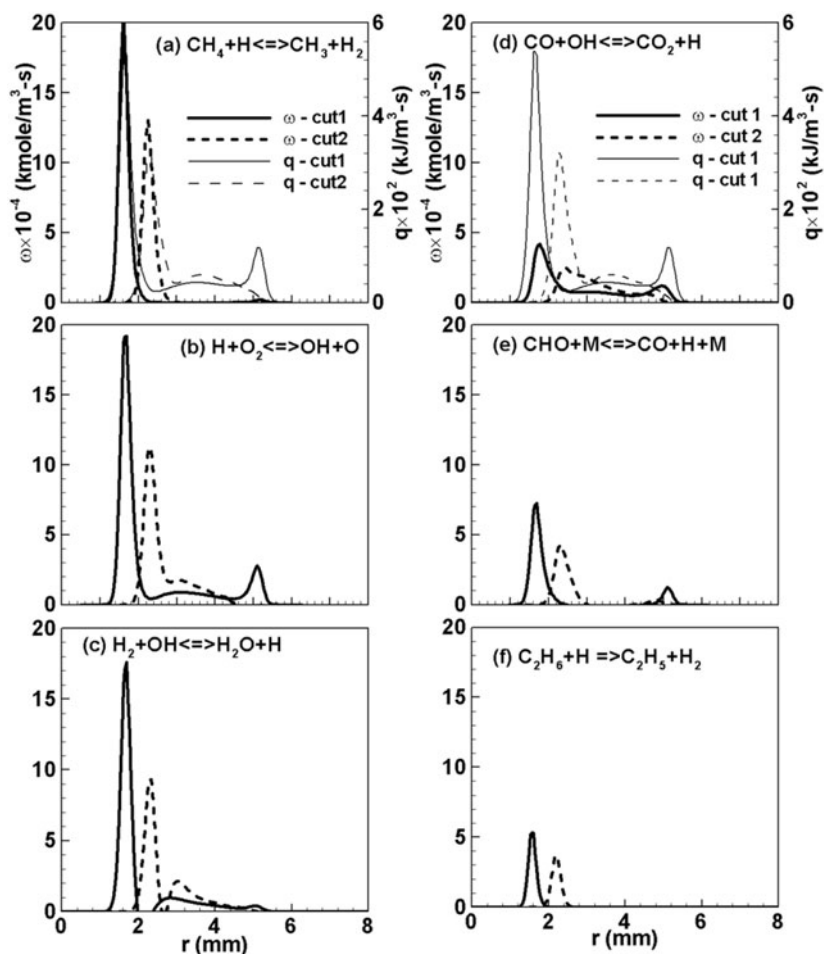


Figure 16 presents the spatial profiles of these reactions along two radial displacements at  $t = 24$  ms (cut 1) and 40 ms (cut 2). For both times, the radial locations pass through the flame approximately 2.5 mm above the triple point as indicated in figure 6. Figures 16(a) and (d) also include the heat release rate profiles along the two cuts, which clearly indicate the transition from a triple flame structure to a double flame structure. The heat release rate profile along cut 1 indicates a triple flame, with the RP, NP, and LP zones located at  $r = 2.8$  mm, 3.5 mm, and 5.2 mm, respectively, while the corresponding profile along cut 2 shows primarily a double flame, but with a relatively wide tail (from  $r = 3.0$  to 5.2 mm) indicating that the LP zone is in the process of extinction or merging with the NP zone.

The reaction rate profiles in figure 16 clearly indicate that a triple flame structure exists at cut 1, which undergoes transition to a double flame structure at cut 2. Reaction (R1) is dominant in the RP zone, since most of the fuel is consumed there, but also has a non-negligible value in the LP zone, as shown along cut 1 in figure 16(a). However, along cut 2, this reaction exhibits a single peak that corresponds to the RP flame. Similarly, reactions (R2) and (R5) are generally dominant in the RP and LP zones [40], as shown by their profiles along cut 1 in



**Figure 16.** Radial profiles of the net reaction rates of six dominant reactions along two transverse cuts shown in figure 6. Cut 1 (---) is at  $t = 24$  ms, and cut 2 (—) at  $t = 40$  ms.

figures 16(b) and (e), while those along cut 2 indicate a double flame structure. Reactions (R3) and (R4) are important in all three reaction zones of a triple flame and, therefore, exhibit double peaks at cut 1 (figures 16(c) and (d)). In contrast, the peak of reaction (R6), involving the formation of ethyl radicals, takes place in the RP zone along both cut 1 and cut 2.

Figures 16(a)–(c) reveal that the net rates of reactions (R1)–(R3) have the largest magnitudes, thereby confirming the importance of fuel decomposition, and chain branching and propagation during flame propagation. We observe from figure 16(d) that the CO/CO<sub>2</sub> reaction (R4) proceeds mainly in the NP region, since it requires hydroxyl radicals that are plentiful there. Although the CO<sub>2</sub> formation reaction has a relatively large heat release rate, its backward rate is also significant, thereby yielding a relatively small net rate [42]. The peaks of the reaction rate of the CHO reaction are in excellent agreement with the heat release rate peaks along cut 1 in figure 16(e). This is in accord with the results of Najm *et al* [43] who found that CHO is a good marker of the heat release rate. Ethane is mainly produced through the reaction of methyl radicals [26], i.e.  $\text{CH}_3 + \text{CH}_3 \Rightarrow \text{C}_2\text{H}_6$ , and it is consumed just ahead of the RP reaction zone (cf figure 16(f)).

#### 4. Conclusions

The characteristics of a propagating triple flame and of the transition from a triple flame structure to a double flame structure in the near field of a jet were investigated both experimentally and numerically. The flame propagation process was recorded using a high-speed camera. Numerical simulations were based on a comprehensive, time-dependent computational model, which employs a detailed description of methane–air chemistry and transport properties. A detailed numerical investigation was performed to characterize the effect of grid size on flame propagation.

There is good qualitative agreement between the measured and predicted flame propagation characteristics, which includes (i) the global features such as flame topology, (ii) temporal characteristics such as flame location with respect to time, (iii) global flame propagation speed in laboratory coordinates *versus* axial distance, and (iv) the location where transition occurs from a propagating to a burner stabilized edge flame structure. The simulations indicate that the flame leading edge or triple point, which can be defined by the intersection of the stoichiometric mixture fraction line and the specific OH contour, propagates along the stoichiometric mixture fraction line. This result is in accord with previous investigation concerning flame lift-off and downstream propagation.

As the flame propagates upstream, the flame propagation speed decreases linearly. However, the axial flamefront propagation velocity in laboratory coordinates remains nearly constant above  $z = 8$  mm, but decreases rapidly below that location. Near the burner wall, the flame curvature increases to two times the value of its downstream freely propagating counterpart. During the propagation process, the curvature-induced stretch dominates over the hydrodynamic stretch. The flame speed decreases with increasing fuel mixture fraction gradient and overall stretch rate, in accord with previous measurements.

Following ignition, a vortex forms ahead of the ignition kernel. The ignition kernel subsequently develops into a triple flame and the vortex is dissipated as this flame propagates upstream. The flame proceeds into the unburned gases and behaves much like a solid body travelling against the incoming flow. When the flame approaches the burner wall, the mixture fraction gradient increases and the LP wing of the triple flame diminishes in size and finally merges with the NP wing to form a double flame. By examining the net reaction rates of major reactions, the transition process can be identified. The differences in the locations of the peak reaction rates illustrate the transition from a triple flame to a burner-stabilized double flame. The spatial profile of key reactions changes from one containing two peaks to a single peak and the flame thickness simultaneously decreases, since the mixing layer thickness diminishes as the flame approaches the burner. As expected, fuel decomposition and chain branching and propagation are found to be important during flame propagation.

#### Acknowledgment

This research was supported by the National Science Foundation Combustion and Plasma Systems Program for which Dr Farley Fisher is the Program Director, and by the NASA Microgravity Research Division for which Dr Uday Hegde serves as the technical monitor. We thank Claudya Arana and Mirko Barbir for assisting with the experiments.

#### References

- [1] Phillips H 1965 *Proc. Combust. Inst.* **10** 1277–83
- [2] Vervisch L 2000 *Proc. Combust. Inst.* **28** 11–24

- [3] Kioni P N, Rogg B, Bray K N C and Liñán A 1993 *Combust. Flame* **95** 276–90
- [4] Plessing T, Terhoeven P, Peters N and Mansour M S 1998 *Combust. Flame* **115** 335–53
- [5] Flynn P F, Durrett R P, Hunter G L, Loye A O, Akinyemi O C, Dec J E and Westbrook C K 1999 *SAE Paper* 1999-01-0509
- [6] Buckmaster J 1996 *Combust. Sci. Technol.* **115** 41–68
- [7] Buckmaster J 2002 *Prog. Energy Combust. Sci.* **28** 435–75
- [8] Hartley L J and Dold J W 1991 *Combust. Sci. Technol.* **80** 23–46
- [9] Ruetsch G R, Vervisch L and Liñán A 1995 *Phys. Fluids* **7** 1447–54
- [10] Chen J-Y and Echehki T 2001 *Combust. Theory Modelling* **5** 499–515
- [11] Wichman I S 1999 *Combust. Flame* **117** 384–93
- [12] Fernandez E, Kurdyumov V and Liñán A 2000 *Proc. Combust. Inst.* **28** 2125–32
- [13] Im H G and Chen J H 2001 *Combust. Flame* **126** 1384–92
- [14] Watson K A, Lyons K M, Donbar J M and Carter C D 1999 *Combust. Flame* **117** 199–271
- [15] Su L K, Han D and Mungal M G 2000 *Proc. Combust. Inst.* **28** 327–34
- [16] Takahashi F, Schmoll W J and Katta V R 1998 *Proc. Combust. Inst.* **27** 675–84
- [17] Ko Y S and Chung S H 1999 *Combust. Flame* **118** 151–63
- [18] Lee B J, Cha M S and Chung S H 1997 *Combust. Sci. Technol.* **127** 55–70
- [19] Shu Z, Aggarwal S K, Katta V R and Puri I K 1997 *Combust. Flame* **111** 276–95
- [20] Siegel R and Howell J R 1981 *Thermal Radiation Heat Transfer* (New York: Hemisphere)
- [21] Smith N, Gore J, Kim J and Tang Q 2001 *Radiation Models, International Workshop on Measurement and Computation of Turbulent Nonpremixed Flames* <http://www.ca.sandia.gov/tdf/Workshop/Submodels.html>
- [22] Qin X, Puri I K, Aggarwal S K and Katta V R 2004 Gravity, radiation and coflow effects on partially premixed flames *Phys. Fluids* at press
- [23] Reid R C, Prausnitz J M and Poling B E 1987 *The Properties of Gases and Liquids* (New York: McGraw-Hill) pp 407–10
- [24] Peters N 1993 *Reduced Kinetic Mechanisms for Applications in Combustion Systems (Lecture Notes in Physics)* ed N Peters and B Rogg (Berlin: Springer) p 3
- [25] Xue H and Aggarwal S K 2001 *AIAA J.* **39** 637–45
- [26] Shu Z, Katta V R, Puri I K and Aggarwal S K 2000 *Combust. Sci. Technol.* **157** 185–211
- [27] Katta V R, Goss L P and Roquemore W M 1994 *Combust. Flame* **96** 60–74
- [28] Chung S H and Law C K 1984 *Combust. Flame* **55** 123–5
- [29] Candel S M and Poinso T 1990 *Combust. Sci. Technol.* **70** 1–15
- [30] Zhong R, Elghobashi S E and Boratov O N 2000 *Phys. Fluids* **12** 2091–100
- [31] Najm H N and Wyckoff P S 1997 *Combust. Flame* **110** 92–112
- [32] De Goey L P H, Mallens R M M and Ten Thije Boonkkamp J H M 1997 *Combust. Flame* **110** 54–66
- [33] Im H G and Chen J H 1999 *Combust. Flame* **119** 436–54
- [34] Qin X, Puri I K and Aggarwal S K 2002 *Proc. Combust. Inst.* **29** 1565–72
- [35] Bilger R W 1988 *Proc. Combust. Inst.* **22** 475–88
- [36] Aggarwal S K and Puri I K 1998 *AIAA J.* **36** 1190–9
- [37] Puri I K, Aggarwal S K, Ratti S and Azzoni R 2001 *Combust. Flame* **124** 311–25
- [38] Kee R J, Grcar J F, Smooke M D and Miller J A 1987 *Sandia Report SAND85–8240*
- [39] Law C K 1993 *Reduced Kinetic Mechanisms for Applications in Combustion Systems (Lecture Notes in Physics)* ed N Peters and B Rogg (Berlin: Springer) p 15
- [40] Azzoni R, Ratti S, Aggarwal S K and Puri I K 1999 *Combust. Flame* **119** 23–40
- [41] Law C K and Sung C J 2000 *Prog. Energy Combust. Sci.* **26** 459–505
- [42] Lee K Y, Cha D J, Hamins A and Puri I K 1996 *Combust. Flame* **104** 27–40
- [43] Najm H N, Paul P H, Mueller C J and Wyckoff P S 2000 *Combust. Flame* **113** 312–32